Article:
Zhang, J, Wang, Y, Zhou, G et al. (2024) Integrating physical and data-driven system frequency response modelling for wind-PV-thermal power systems. IEEE Transactions on Power Systems, 39 (1). pp. 217-228. ISSN: 0885-8950

https://doi.org/10.1109/tpwrs.2023.3242832

Integrating physical and data-driven system frequency response modelling for wind-PV-thermal power systems

Jianhua Zhang, *Member*, *IEEE*, Yongyue Wang, Guiping Zhou, Lei Wang, Bin Li and Kang Li, *Senior Member*, *IEEE*

***Abstract*—This paper presents an integrated system frequency response (SFR) modelling method for wind-PV-thermal power systems (WPTPSs) by combining physical model-driven and data-driven modelling method. The SFR physical model is built and simplified by the balanced truncation (BT) method. Based on the physical model, an improved radial basis function neural networks (RBFNNs) is then employed to establish an off-line SFR model using source data. Following the transfer learning method, the transferred data from the source data set is determined by the maximum mean discrepancy (MMD) criterion. The RBFNNs-based SFR model is then fine-tuned using the transferred source data and target data. Finally, the fine-tuned RBFNNs is applied to investigate real-time SFR of WPTPSs. Simulation results testify the effectiveness of the proposed SFR modelling strategy for an illustrative WPTPS.**

***Index Terms*—Data-driven modelling, neural networks, physical model, primary frequency control, renewable energy, system frequency response, transfer learning.**

I. Introduction

THE imbalance between power generation and load causes frequency deviation. With the energy transition towards carbon neutrality, high-penetration renewable energy sources will connect to power grid. This poses some new operation and generation challenges. Apart from the reduced system inertia, the stochastic fluctuations induced by photovoltaic (PV) power plants and wind power plants lead to the randomness and volatility of power generation. Hence, the characteristics and operating state of the wind-PV-thermal power system (WPTPS) change dynamically. In this context, it is crucial to investigate system frequency response (SFR) [1, 2].

The SFR model of a WPTPS can facilitate a quick and quantitative study of the frequency response characteristics without simulating the complex WPTPS. The SFR model reveals the dynamic relationship between the additional active variation and the frequency deviation. Compared with the standard dynamical system identification, the SFR model can be employed to evaluate the inertial and droop responses of a TPWPS.

In order to study the dynamic characteristics of system frequency under the disturbance of generation or load, some approaches to SFR modelling have been presented in terms of physical modelling, data-driven modelling, and integrating physical and data-driven modelling.

Physical modelling method has been widely used to analyze the system frequency dynamics [3-11]. Chan et al. built the average system frequency model for the first time, the average system frequency behavior of a multi-generator system was modelled to investigate the effects of governor-turbine dynamics on SFR following a major loss of generation, three kinds of models were built in terms of delay model, canonical model and integrating delay and canonical model [3]. Then Anderson and Mirheydar further established a low-order SFR model by neglecting nonlinearities and small time constants in the equations of the generating units of the power system [4]. Afterward, the analytic SFR model presented in [4] was applied to investigate the aggregated load-frequency behavior following a contingency in isolated power systems [5]. Following the physical model in [4], the multi-machine SFR model was aggregated into a single-machine model [6]. Apart from these SFR physical models built for thermal power plants, more recent studies were proposed to establish physical models for wind power plants [7-12] and PV power plants [13], respectively. An analytical model was proposed to investigate inertia and droop responses for a wind farm connected to power grid [7]. A low-order SFR model was established for power systems with high penetration of wind power plants [8]. An extended SFR model was built for high penetration of wind power, in which the operating regions and wind speed disturbance were taken into account [9]. An SFR model was proposed to analyze the system frequency dynamics of large-scale power systems with high penetration of wind energy [10]. An SFR modelling method was provided for a power system

This work was supported in part by National Key R&D Program of China No.2019YFB1505400. (Corresponding author: Jianhua Zhang)

J. H. Zhang is with the State Key Laboratory of Alternate Electrical Power System with Renewable Energy Sources, North China Electric Power University, Beijing, 102206, China (email: zjh@ncepu.edu.cn).

Y. Y. Wang is with the School of Control and Computer Engineering, North China Electric Power University, Beijing, 102206, China

G. P. Zhou, L. Wang and B. Li are with the State Grid Liaoning Electric Power Supply Co. Ltd., Shenyang, 110006, China.

K. Li is with School of Electronic and Electric Engineering, University of Leeds, LS2 9JT, UK

Color versions of one or more of the figures in this paper are available online at http://ieeexplore.ieee.org.

composed of a wind power plant with Type 3 wind turbines and a thermal power plant with a synchronous generator. Based on the mass-spring-damping concept, the uniform SFR model was then obtained [11]. By adding new constraints, the SFR model was employed to integrate wind power plants into power systems within the framework of security-constrained unit commitment[12]. A small-signal PV system model was presented to design frequency support control systems [13]. In practical WPTPSs, there are nonlinearities in wind/PV/thermal power plants. Besides, there exist nonlinearities in power electronic interfaces by which renewable energy power plants are connected to power grid. In addition, renewable energy power plants induce non-Gaussian disturbances. The above-mentioned physical modelling methods are clear in logistics and rigorous in derivation, but some necessary assumptions and rational simplifications are needed. These SFR modelling methods can't deal with nonlinearities and stochastic disturbances well. Obviously, the accuracy of the established physical models limits their application in engineering practice.

Recently, several data-driven SFR modelling methods were proposed to cope with nonlinearities and disturbances. A transfer function identification method was presented to investigate a load frequency regulation oriented thermal power unit's dynamic model, in which a two-stage procedure is used to reduce both noise effects and the order of the transfer function [14]. The power system frequency response can be estimated from ambient synchrophasor measurements, the analytical conditions were developed for establishing the equivalence between the cross correlation of ambient generator speed data and the SFR between any two locations [15]. Support vector regression was employed to estimate the minimum frequency and dynamic SFR of a disturbed power system [16]. Based on survival information potential (SIP) criterion, an improved radial basis function neural network (RBFNN) was presented to build the equivalent model of wind-thermal integrated power systems [17]. Although nonlinearities and uncertainties of the SFR might be revealed using the above data-driven modelling methods, however, their accuracy depends on the quantity and quality of the database. These data-driven SFR modelling methods can obtain the SFR model in the vicinity of certain scenarios based on the collected input-output data. Nevertheless, the established data-driven models can't reveal the dynamics of the power system in other scenarios due to lacking knowledge transferability.

When physical modelling and data-driven modelling methods are used alone, the obtained SFR model performance is not necessarily satisfactory. A complete and effective SFR modelling method is expected by integrating the advantages of physical model-driven methods in causality processing and data-driven methods in high-efficiency correlation analysis. Previous work hardly investigates integrated SFR modelling methods by combining physical models with data-driven models. More recently, an SFR modelling method was proposed by integrating a physical model and a data-driven model [18]. Based on statistical data, the uncertain variabilities in power systems were modelled using Monte Carlo simulation. The uncertain variabilities induced by measurement, communication, generation, and load were all regarded as additive disturbances. Although stochastic disturbances are considered in [18], the stochastic model added to the conventional SFR physical model is linear.

Up till now, little research has focused on hybrid power plants connected to power grid except that in Ref. [11-12]. Motivated by these investigations, this work deals with integrated SFR modelling methods for WPTPSs. Considering the drawbacks of previous methods, a novel SFR modelling approach is proposed for WPTPSs by integrating its physical model with a data-driven model. The proposed approach exploits a reduced-order physical model to screen critical features for a subsequent data-driven model. Inspired by neural networks-based system identification and transfer learning (TL), the data-driven SFR modelling method is presented by combining an improved RBFNNs with TL. Neural networks-based system identification methods have been used to model complex processes or systems with nonlinearities and uncertainties and demonstrated their versatility and effectiveness [19-20]. In particular, the improved RBFNNs-based system identification approaches were presented and applied in [17, 21-25]. Along this line of consideration, an improved radial basis function neural network (RBFNN) is utilized to build a data-driven model in this work, which deals with non-Gaussian disturbances from PV and wind power plants. The knowledge transferability obtained by TL can be found in [26-28]. Accordingly, TL is introduced to enhance the learning performance of the RBFNNs. The SFR knowledge of the WPTPS operating in other scenarios can be transferred without much expensive data-collecting effort.

The major contributions of this paper lie in:

1) An integrated SFR modelling scheme is proposed for WPTPSs by combining a physical model and a data-driven model. Physical and data-driven SFR modelling is implemented in sequence.
2) The balanced truncation (BT) method is employed to reduce the order of the SFR physical model, which decreases the input feature dimensions of the data-driven model. Accordingly, the learning efficiency and flexibility of the RBFNNs-based SFR modelling method can be improved.
3) The improved RBFNNs deals with non-Gaussian disturbances from PV and wind power plants when training RBFNNs based on the SIP of frequency deviation.
4) A data-driven SFR modelling method is presented by incorporating TL into the improved RBFNNs. The maximum mean discrepancy (MMD) criterion is used to improve the transferability of the RBFNNs-based pre-trained SFR model.

The rest of the paper is organized as follows. Section II proposes an integrated SFR modelling scheme for a WPTPS by combing a physical model, an improved RBFNNs, and transferred knowledge together. Section III presents the integrated SFR modelling method. Section IV conducts the simulation research on SFR modelling for an illustrative WPTPS. Section V concludes this paper.

II. Integrated SFR Modelling Scheme For WPTPSs

This section introduces the integrated SFR modelling scheme and the WPTPS shown in Fig. 1. Moreover, the four-stage implementation of the integrated SFR modelling method is shown in Fig. 2.

Figure 1 shows the integrated SFR modelling schematic diagram for a WPTPS. The power system is composed of 1) the wind power plant consists of p wind turbines based on doubly fed induction generator (DFIG) and their primary frequency regulation; 2) The PV power plant includes q photovoltaic panels and their primary frequency regulation; 3) The thermal power plant includes r synchronous generators and their primary frequency regulation control and 4) Local load.

The dynamic behavior of WPTPSs is complicated in terms of time-varying, nonlinearities, uncertainties, intermittence, and

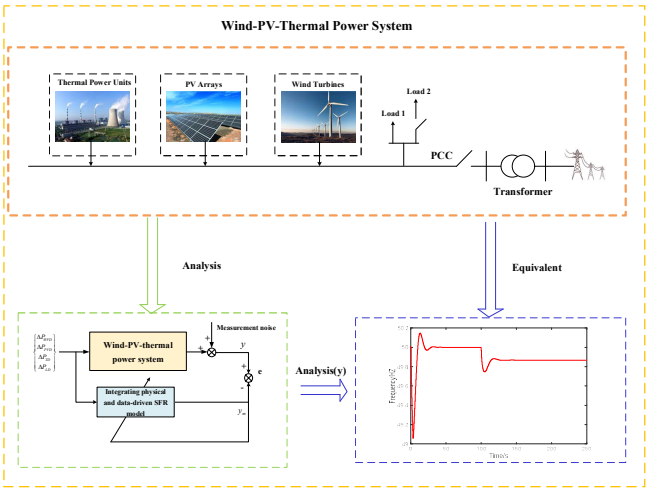

Fig. 1. Schematic diagram of building the model.

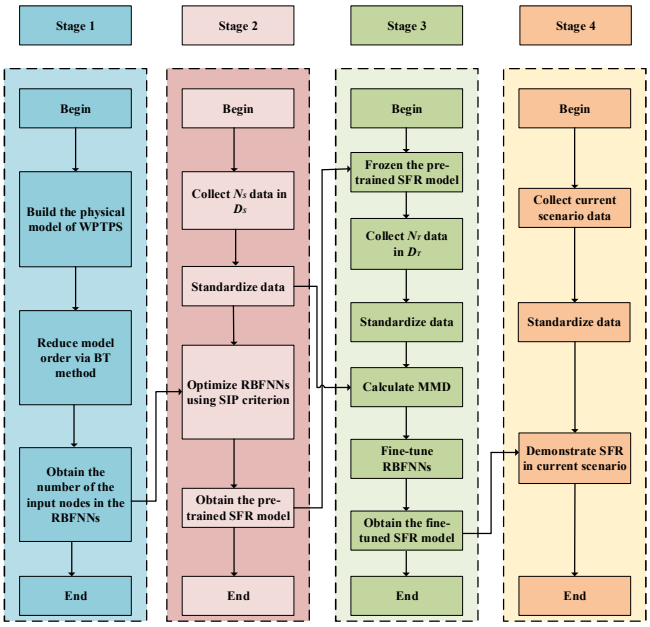

Fig. 2. Integrated SFR modelling scheme.

so on. Therefore, an integrated SFR modelling scheme is presented for WPTPSs in this section.

The goal is to establish an SFR model by integrating physical and data-driven modelling approaches. The dynamic frequency response characteristics of WPTPSs can then be accurately and quickly analyzed under the time scale of primary frequency regulation. The collected input data includes the input power, the wind farm power, the photovoltaic power, the mechanical power of the thermal power plant, and the load. The collected output signal y is the system frequency deviation at the point of common coupling (PCC) shown in Fig. 1. y_m represents the modelling output, and $e = y - y_m$ is the modelling error.

As shown in Fig. 2, the integrated SFR modelling process is composed of 4 stages: 1) Building the physical model at beginning stage; 2) Improving RBFNNs at offline stage; 3) Fine-tuning the RBFNNs at offline stage, and 4) Applying the fine-tuned RBFNNs to the WPTPS at online stage.

III. Integrated SFR Modelling Method

This section presents the four-stage hybrid SFR modelling method in detail. Finally, the procedures to implement the proposed integrated SFR modelling approach are summarized.

A. Physical Model

In order to sift critical features for the subsequent data-driven model, the input/output orders of the SFR physical model need to be reduced. Specifically, the input nodes of the RBFNNs-based data-driven SFR model can be determined according to the reduced-order SFR physical model.

Although the reduced model of a WPTPS can be obtained based on the high-order, high-fidelity SFR physical model, slow system dynamics of the boiler and the fast generator dynamics are usually ignored for power system frequency analysis and control design. Hence, a reduced model of a WPTPS can be developed using the simplified SFR model shown in Fig. 3.

The simplified transfer functions of the thermal power plant, the PV plant and the wind plant are formulated. The overall SFR physical model is then established for the WPTPS. Afterward, the order of the physical model is reduced by the balanced

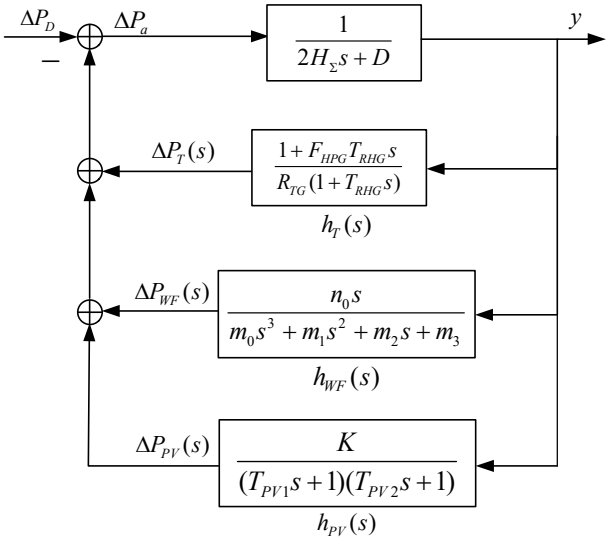

Fig. 3. Block diagram of a WPTPS using the simplified SFR model.

truncation (BT) method. The simplified SFR physical model can then be obtained at stage 1.

The block diagram of a WPTPS is shown in Fig. 3, where $h_T(s)$, $h_{PV}(s)$, and $h_{WF}(s)$ are the transfer functions of a thermal power unit, PV plant, and wind plant respectively. $\Delta P_T(s)$, $\Delta P_{PV}(s)$, and $\Delta P_{WF}(s)$ stand for the output power changes of the thermal power unit, PV plant, and wind power plant for frequency regulation respectively. H_Σ and D are the equivalent inertia constant (seconds) and the equivalent load damping coefficient, respectively.

The overall generator-load dynamic relationship between the incremental mismatch power $\Delta P_a(s)$ and the frequency deviation can be described by

$$\frac{y(s)}{\Delta P_a(s)} = \frac{1}{2H_\Sigma s + D} \tag{1}$$

where $\Delta P_a(s) = \Delta P_T(s) + \Delta P_{WT}(s) + \Delta P_{PV}(s) - \Delta P_D(s)$, $\Delta P_D(s)$ is the overall generator-load disturbances.

Several low-order models for the representation of a thermal power plant, PV plant, and wind plant have been proposed to analyse power system frequency and design frequency regulation systems [29-31].

Taking the mechanical power change as the output and the system frequency deviation as the input, a simplified turbine governor model of a single reheat thermal power unit can be obtained [29].

$$h_T(s) = \frac{\Delta P_T(s)}{y(s)} = \frac{1 + F_{HPG}T_{RHG}s}{R_{TG}(1 + T_{RHG}s)} \tag{2}$$

where R_{TG} is the adjustment coefficient of the steam turbine governing system. T_{RHG} stands for the parameter of the reheater time constant. F_{HPG} represents the power proportion of high-pressure turbine stage of the thermal power unit.

The change of wind speed will affect the operating state of the DFIG wind turbine. In order to investigate the primary frequency response of each wind turbine generator in a wind plant, it can be assumed that the speed difference of each wind turbine generator is small, as a result, the speed is approximately equal to the average speed. In addition, the system frequency deviation signal detected by each wind turbine is nearly identical. Therefore, the parameter aggregation method based on weighted dynamic equivalence can be utilized to establish the transfer function of the wind plant. The aggregated transfer function of the wind plant can be described by [30]

$$h_{WF}(s) = \frac{\Delta P_{WF}(s)}{y(s)} = \frac{n_0 s}{m_0 s^3 + m_1 s^2 + m_2 s + m_3} \tag{3}$$

where the model parameters can be obtained in [30].

The aggregated transfer function of a PV plant can be formulated by [31]

$$h_{PV}(s) = \frac{\Delta P_{PV}(s)}{y(s)} = \frac{K}{(T_{PV1}s + 1)(T_{PV2}s + 1)} \tag{4}$$

where K is the droop gain of the PV plant. T_{PV1} represents the time when the frequency regulation command from the power control system of the PV plant is sent to the inverter. T_{PV2} stands for the execution time of the inverter.

The frequency deviation can be expressed by following SFR physical model:

$$\frac{y(s)}{\Delta P_D(s)} = \frac{a_6 s^6 + a_5 s^5 + a_4 s^4 + a_3 s^3 + a_2 s^2 + a_1 s + a_0}{b_7 s^7 + b_6 s^6 + b_5 s^5 + b_4 s^4 + b_3 s^3 + b_2 s^2 + b_1 s + b_0} \tag{5}$$

Based on the model (5), BT method proposed by Moore [32] is used to build a reduced-order SFR model with sufficient accuracy. The model can be reformulated by the following state-space model

$$\begin{aligned} \dot{\boldsymbol{x}} &= \boldsymbol{A}\boldsymbol{x} + \boldsymbol{B}u \\ y &= \boldsymbol{C}\boldsymbol{x} \end{aligned} \tag{6}$$

where $\boldsymbol{A} \in \mathbb{R}^{7\times 7}$, $\boldsymbol{B} \in \mathbb{R}^{7\times 1}$ and $\boldsymbol{C} \in \mathbb{R}^{1\times 7}$ are the system, input, and output matrices with proper dimensions. The BT procedure is centered around information obtained from the controllability Gramian $\boldsymbol{W}_C$ and observability Gramian $\boldsymbol{W}_O$. Two Gramians can be solved by the following Lyapunov equations

$$\begin{cases} \boldsymbol{A}\boldsymbol{W}_C + \boldsymbol{W}_C\boldsymbol{A}^T + \boldsymbol{B}\boldsymbol{B}^T = 0 \\ \boldsymbol{A}^T\boldsymbol{W}_O + \boldsymbol{W}_O\boldsymbol{A} + \boldsymbol{C}^T\boldsymbol{C} = 0 \end{cases} \tag{7}$$

By finding a similarity transformation $\boldsymbol{T}$, balanced realization is obtained such that

$$\boldsymbol{T}^T\boldsymbol{W}_C\boldsymbol{T} = \boldsymbol{T}^{-1}\boldsymbol{W}_O\boldsymbol{T}^{-T} = \mathrm{diag}\left(\sigma_1, \sigma_2, \ldots, \sigma_{\bar{n}}\right) \tag{8}$$

where $\sigma_1 \geq \sigma_2 \geq \cdots \geq \sigma_{\bar{n}} > 0$ are Hankel singular values of the system. Hence, the system in the new realization can be given by

$$G(s) \sim \begin{bmatrix} \boldsymbol{T}^{-1}\boldsymbol{A}\boldsymbol{T} & \boldsymbol{T}^{-1}\boldsymbol{B} \\ \boldsymbol{C}\boldsymbol{T} & \boldsymbol{D} \end{bmatrix} = \begin{bmatrix} \hat{\boldsymbol{A}} & \hat{\boldsymbol{B}} \\ \hat{\boldsymbol{C}} & \boldsymbol{D} \end{bmatrix} = \begin{bmatrix} \hat{\boldsymbol{A}}_{11} & \hat{\boldsymbol{A}}_{12} & \hat{\boldsymbol{B}}_1 \\ \hat{\boldsymbol{A}}_{21} & \hat{\boldsymbol{A}}_{22} & \hat{\boldsymbol{B}}_2 \\ \hat{\boldsymbol{C}}_1 & \hat{\boldsymbol{C}}_2 & \boldsymbol{D} \end{bmatrix} \tag{9}$$

We select the $\bar{r}$ states related to the $\bar{r}$ largest Hankel singular values, the $\bar{r}^{th}$ order reduced model $G_{\bar{r}}(s)$ can then be obtained as follows:

$$G_{\bar{r}}(s) \sim \begin{bmatrix} \hat{\boldsymbol{A}}_{11} & \hat{\boldsymbol{B}}_1 \\ \hat{\boldsymbol{C}}_1 & \boldsymbol{D} \end{bmatrix} \tag{10}$$

Following the simplified SFR physical model (10), lower input and output orders of the SFR model, $\bar{m}$ and $\bar{n}$, are known. Consequently, both input and hidden nodes of the RBFNNs can be further decreased.

B. Data-driven model

In this section, the data-driven SFR model is implemented by an improved RBFNNs. First, the improved RBFNNs is employed to obtain the pretrained SFR model using source data at stage 2. The fine-tuned SFR model is then obtained at stage 3 by combining the pretrained RBFNNs model and TL.

Following the developments of RBFNNs [17, 21-25], an $n - \bar{n}_h - 1$ RBFNNs is utilized to build the data-driven model for the WPTPS. Denote $\boldsymbol{x}$ and $y_m(k)$ as the input and output of RBFNNs, respectively. The input consists of the sequence of

the disturbances and the measured frequency deviation.

$$\begin{aligned}\boldsymbol{x} = [&\Delta P_{LD}(k),...\Delta P_{LD}(k-\bar{m}),\Delta P_{TD}(k),...\Delta P_{TD}(k-\bar{m}),\\ &\Delta P_{WFD}(k),...\Delta P_{WFD}(k-\bar{m}),\Delta P_{PVD}(k),...\Delta P_{PVD}(k-\bar{m}),\\ &y(k),...y(k-\bar{n})]^T \in \mathbb{R}^{n\times 1}\end{aligned}$$

where the number of the input nodes is $n = 4\bar{m}+\bar{n}+5$. The identified frequency deviation $y_m(k)$ can be described by

$$y_m(k) = \sum_{j=1}^{\bar{n}_h} \omega_j(k-1) R_j(\boldsymbol{x}(k)) \tag{11}$$

where ω_j is the connection weight between hidden layer and output layer. The output of the j^{th} hidden node is

$$R_j(\boldsymbol{x}(k)) = \exp\left(-\frac{\left\|\boldsymbol{x}(k)-\boldsymbol{c}_j(k-1)\right\|^2}{2b_j^2(k-1)}\right) \tag{12}$$

where $\boldsymbol{c}_j \in \mathbb{R}^{n\times 1}$ denotes the center vector of the j^{th} hidden neuron. $\left\|\boldsymbol{x}(k)-\boldsymbol{c}_j(k-1)\right\|$ is the Euclidean distance between $\boldsymbol{x}$ and $\boldsymbol{c}_j$. b_j stands for the radius or width of the j^{th} hidden neuron.

Power grids are impacted by multiple kinds of disturbances induced by varying demands, grid-connected renewable power, and energy trading. The frequency time series of power grids in North America, Japan, and Europe were investigated in [33], in which the power grid frequency fluctuations are non-Gaussian. With the advancement of information theoretic learning techniques, some statistical indices have been used to investigate system identification, filtering, and control strategies of non-Gaussian systems, such as entropy, correntropy, high order moments, SIP, and so on [34-38]. The SIP of a random variable is defined in terms of the survival function instead of the probability density function (PDF) [36]. The SIP criterion outperforms the widely used minimum error entropy criterion when dealing with non-Gaussian disturbances [37-38]. For example, it is easy to estimate and has no translation invariance. Therefore, the SIP criterion is applied to train RBFNNs in this work.

At instant k, the identification error $e(k) = y(k) - y_m(k)$ is collected using a sliding window whose width is L, the identification error is reformulated in ascending order of magnitude, $0 \le e(k)_1 \le e(k)_2 \le ... \le e(k)_L$, and then the α order SIP of the identification error can be calculated by

$$\begin{aligned}\hat{S}_\alpha(e(k)) &= \int_0^\infty \left(\frac{1}{L}\sum_{i=1}^{L} \iota(|\, e(k)_i \,| > e)\right)^\alpha de\\ &= \sum_{j=1}^{L} \int_{|e(k)_{j-1}|}^{|e(k)_j|} \left(\frac{1}{L}\sum_{i=1}^{L} \iota(|\, e(k)_i \,| > e)\right)^\alpha de\\ &= \sum_{j=1}^{L} \left(\frac{L-j+1}{L}\right)^\alpha \left(|\, e(k)_j \,| - |\, e(k)_{j-1} \,|\right)\end{aligned} \tag{13}$$

where the order $\alpha > 0$. $\iota(\cdot)$ is an indicator function. $\iota(\bar{A}) = 1$ when $\bar{A}$ is true, and $\iota(\bar{A}) = 0$ when $\bar{A}$ is false. Let $e(k)_0 \triangleq 0$, Eq. (13) can be reformulated as follows:

$$\begin{aligned}\hat{S}_\alpha(e(k)) &= \left(1-\left(\frac{L-1}{L}\right)^\alpha\right)|e(k)_1| + \cdots\\ &+ \left(\left(\frac{2}{L}\right)^\alpha - \left(\frac{1}{L}\right)^\alpha\right)|\, e(k)_{L-1} \,| + \left(\frac{1}{L}\right)^\alpha |\, e(k)_L \,|\\ &= \sum_{j=1}^{L} \lambda_j |e(k)_j|\end{aligned} \tag{14}$$

where $\lambda_j = \left(\frac{L-j+1}{L}\right)^\alpha - \left(\frac{L-j}{L}\right)^\alpha$.

In this paper, $\alpha = 2$, the quadratic SIP of the squared identification error is used to train the RBFNNs

$$E(k) = \hat{S}_\alpha(e^2(k)) = \sum_{j=1}^{L} \lambda_j e^2(k)_j \tag{15}$$

The training rules of the weights between the hidden neurons and the output neuron, ω_j, are formulated by the gradient descent method

$$\omega_j(k) = \omega_j(k-1) + \Delta\omega_j(k) + \bar{\alpha}(\omega_j(k-1) - \omega_j(k-2)) \tag{16}$$

$$\begin{aligned}\Delta\omega_j(k) &= -\eta\frac{\partial E(k)}{\partial \omega_j(k-1)} = -\eta\frac{\partial E(k)}{\partial e(k)}\frac{\partial e(k)}{\partial y_m(k)}\frac{\partial y_m(k)}{\partial \omega_j(k-1)}\\ &= 2\eta\sum_{j=1}^{L} \lambda_j e(k)_j R_j(x(k))\end{aligned} \tag{17}$$

where $\eta > 0$ is the pre-specified learning factor, $\bar{\alpha} \in [0,\ 1)$ stands for the momentum parameter.

The training of the width of the j^{th} hidden neuron, b_j, can be formulated to give

$$b_j(k) = b_j(k-1) + \Delta b_j(k) + \bar{\alpha}\left(b_j(k-1) - b_j(k-2)\right) \tag{18}$$

where it can be further seen that

$$\begin{aligned}\Delta b_j(k) &= -\eta\frac{\partial E(k)}{\partial b_j(k-1)} = -\eta\frac{\partial E(k)}{\partial R_j(\boldsymbol{x}(k))}\frac{\partial R_j(\boldsymbol{x}(k))}{\partial b_j(k-1)}\\ &= 2\eta\left(\sum_{j=1}^{L} \lambda_j e(k)_j\right)\omega_j(k-1)R_j(\boldsymbol{x}(k))\frac{\left\|\boldsymbol{x}(k)-\boldsymbol{c}_j(k-1)\right\|^2}{b_j^3(k-1)}\end{aligned} \tag{19}$$

The training of the center vector of the j^{th} hidden neuron, $\boldsymbol{c}_j$, can be described by

$$c_{ji}(k) = c_{ji}(k-1) + \Delta c_{ji}(k) + \bar{\alpha}\left(c_{ji}(k-1) - c_{ji}(k-2)\right) \tag{20}$$

where it can be shown that

$$\begin{aligned}\Delta c_{ji}(k) &= -\eta\frac{\partial E(k)}{\partial c_j(k-1)} = -\eta\frac{\partial E(k)}{\partial R_j(\boldsymbol{x}(k))}\frac{\partial R_j(\boldsymbol{x}(k))}{\partial c_j(k-1)}\\ &= 2\eta\left(\sum_{j=1}^{L} \lambda_j e(k)_j\right)\omega_j(k-1)R_j(\boldsymbol{x}(k))\frac{x_i(k)-c_{ji}(k-1)}{b_j^2(k-1)}\end{aligned} \tag{21}$$

Hence, the pre-trained RBFNNs-based SFR model can be obtained by training the data in source domain $\mathcal{D}_S$.

It is worth pointing out that the source data corresponding to typical scenarios can usually be collected from simulation or practical WPTPSs. In this work, the scenario of the WPTPS is characterized by load, solar irradiance and wind speed. The abundant source data, denoted by data in source domain $\mathcal{D}_S$, is used to train the RBFNNs.

When we investigate the WPTPS in the current scenario, some data can also be acquired and denoted by data in the target domain $\mathcal{D}_T$. Although the data both in the source and target domain can be utilized to obtain the online data-driven SFR model, however, unnecessary data updating and retraining are usually very time-consuming. Hence, TL is a very effective method to solve this problem, and the transferred knowledge will be determined based on the MMD criterion at stage 2.

The collected data in the target domain is usually limited. Moreover, the distribution of target domain data may not be the same as that of source domain data. Accordingly, MMD is introduced to measure the distribution difference between source and target data. The definition of MMD is as follows [39]:

$$MMD_b(\bar{p},\bar{q}) = \sqrt{f_1(\boldsymbol{x}^S) + f_2(\boldsymbol{x}^S,\boldsymbol{x}^T) + f_3(\boldsymbol{x}^T)} \tag{22}$$

where $\bar{p}$ and $\bar{q}$ are the distributions of the source and the target domains.

$$f_1(\boldsymbol{x}^S) = \frac{1}{N_S^2}\sum_{i,j=1}^{N_S} \bar{k}\left(\boldsymbol{x}_i^S, \boldsymbol{x}_j^S\right) \tag{23}$$

$$f_2(\boldsymbol{x}^S,\boldsymbol{x}^T) = -\frac{2}{N_S N_T}\sum_{i,j=1}^{N_S,N_T} \bar{k}\left(\boldsymbol{x}_i^S, \boldsymbol{x}_j^T\right) \tag{24}$$

$$f_3(\boldsymbol{x}^T) = \frac{1}{N_T^2}\sum_{i,j=1}^{N_T} \bar{k}\left(\boldsymbol{x}_i^T, \boldsymbol{x}_j^T\right) \tag{25}$$

where N_S and N_T stand for the number of samples in $\mathcal{D}_S$ and $\mathcal{D}_T$ respectively. $\boldsymbol{x}^S \in \mathbb{R}^{1\times N_S}$ and $\boldsymbol{x}^T \in \mathbb{R}^{1\times N_T}$ are the samples in source and target domain respectively. $\bar{k}$ is the kernel function for mapping the values in a reproducing kernel Hilbert space. By the following Gaussian kernel function (26), the MMD leads to zero if the distributions are identical. The smaller the MMD value, the smaller the distribution difference between two domains, and vice versa. The source data with small MMD will be transferred.

$$\bar{k}\left(\boldsymbol{x}^S,\boldsymbol{x}^T\right) = \exp\left(-\frac{1}{2\sigma^2}\left\|\boldsymbol{x}^S - \boldsymbol{x}^T\right\|^2\right) \tag{26}$$

where σ is the width of the Gaussian kernel function.

It should be noted that when the MMD is far greater than the preseted threshold, an accurate SFR model cannot be obtained using the TL technique, so it is necessary to collect appropriate source data and correct the pretrained RBFNNs.

As shown in Fig. 4, the RBFNNs is fine-tuned at stage 3, in which the hidden nodes of the pretrained RBFNNs are frozen. By experimentally adding appropriate hidden nodes to the RBFNNs, the generalization ability of the RBFNNs is improved using transferred source data and target data.

At instant k, the corresponding scenario can be determined according to the current load, solar irradiance and wind speed of the WPTPS. As a result, the SFR can be obtained using the fine-tuned RBFNNs-based SFR model at stage 4.

The flow chart of the four-stage SFR modelling method is shown in Fig. 5.

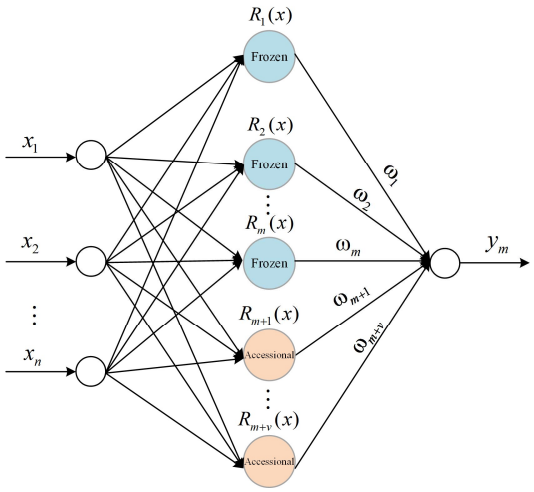

Fig. 4. Fine-tuned RBFNNs-based SFR model

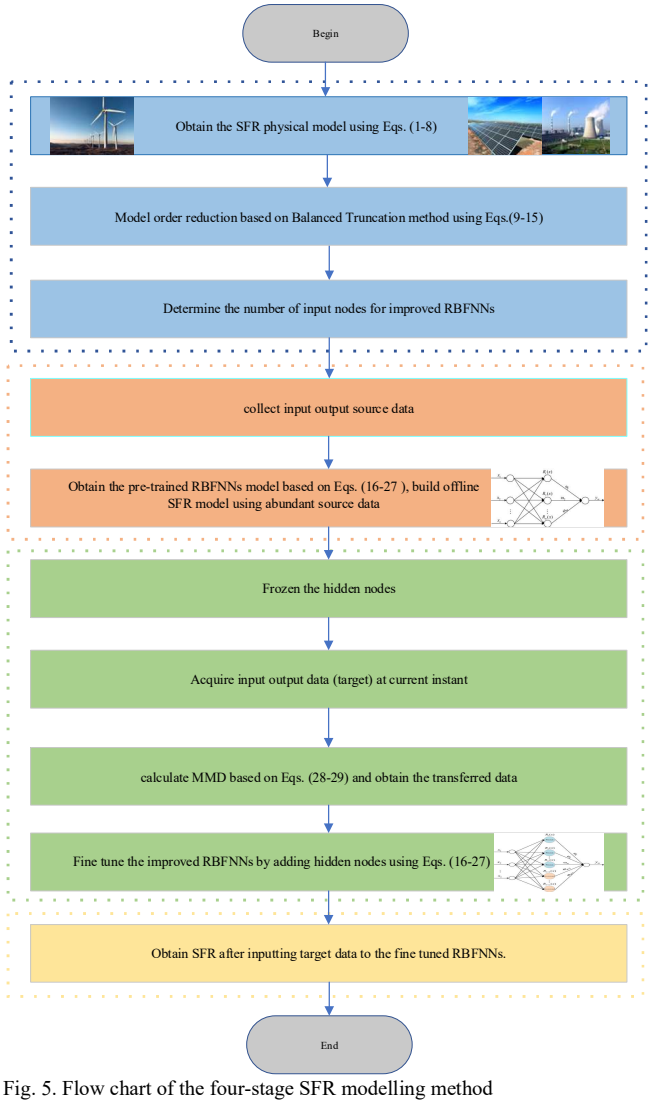

Fig. 5. Flow chart of the four-stage SFR modelling method

IV. Results and Discussions

The following simulations were conducted to test the proposed SFR modelling algorithm. The experimental WSTPS is shown in the upper half of Fig. 1, in which $p = 200$ and $q = r = 2$. There are 200 × 1.5MW DFIG wind turbine generators in the wind farm. Each wind turbine generator adopts the same droop control method. The droop gain is set to $K_{pf} = -50\text{MW/Hz}$. The model parameters of the DFIG wind turbine generator are kept the same as that in [30]. There are two 600MW reheat steam generator units in the thermal power plant. Each reheat steam generator unit is equipped with a prime mover speed control system and an excitation voltage regulator. The adjustment coefficient of the steam turbine governing system is set to $R_{TG} = -0.05\text{Hz/MW}$. The model parameters of the reheat steam generator unit are given in Table I; Besides, the model parameters of the PV plant are shown in Table II. The droop gain is set to $K = -50\text{MW/Hz}$ for the PV plant. In this simulation, the sampling period, the pre-specified learning factor and the momentum parameter are set to $T_s = 0.1s$, $\eta = 0.05$ and $\bar{\alpha} = 0.05$, respectively. The width of the sliding window is set to L=100.

TABLE I
Parameters of Thermal Power Unit

Parameter	Values	Parameter	Values
Governor time constant	0.18s	High-pressure turbine fraction	0.33
Steam chest time constant	0.2s	Governor speed regulation	0.05
Reheat time constant	11.27s	Load damping factor	0.02

TABLE II
Parameters of Photovoltaic Power Station

Parameter	Values	Parameter	Values
DC voltage at photovoltaic array side	300V	DC voltage at inverter side	500V
DC capacitor at photovoltaic array side	1e-4F	DC capacitor at inverter side	6e-3F
Rated power	150MW	Droop control coefficient	50

First, the BT method was used to reduce the order of the SFR physical model, and the input/output orders of the reduced model were reduced to $\bar{m} = \bar{n} = 2$. Fig. 6 compares the bode plots of the SFR physical model and the reduced model, it can be observed from magnitude and phase that the reduced model can approximate the original model (5).

With the aid of BT method, the node number in the input layer of the RBFNNs decrease from 36 to 15. Besides, the hidden nodes can be reduced by trial and error. Hence, the computation burden and complexity of the RBFNNs can be greatly reduced.

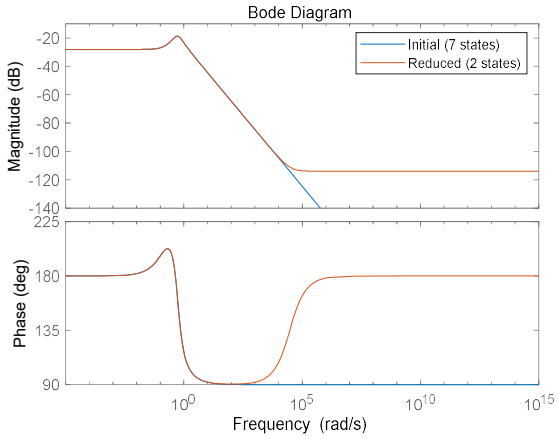

Fig. 6. Bode diagram of original and reduced SFR physical model

Five performance evaluation metrics are employed to assess the accuracy of the identified results in terms of mean square error (MSE), root mean square error (RMSE), standard deviation (SD), mean absolute error (MAE) and the coefficient of determination R^2. When MSE, RMSE, SD and MAE are close to 0, and R^2 approaches 1, the frequency deviation can be identified with proper accuracy.

(1) MSE is the expected value of the square of the difference between the identified frequency deviation and the actual frequency deviation.

$$\text{MSE} = \frac{1}{n}\sum_{i=1}^{n}(y_{mi} - y_i)^2 \tag{27}$$

(2) RMSE, the square root of MSE, evaluates the average identification error, which is intuitive in order of magnitude.

$$\text{RMSE} = \sqrt{\frac{1}{n}\sum_{i=1}^{n}(y_{mi} - y_i)^2} \tag{28}$$

(3) SD reflects the dispersion degree of the identified data set.

$$\text{SD} = \sqrt{\frac{1}{n}\sum_{i=1}^{n}(y_{mi} - \frac{1}{n}\sum_{i=1}^{n}y_{mi})^2} \tag{29}$$

(4) MAE can better reflect the actual situation of the identified frequency deviation and provide a generic and bounded performance measure for the identified results.

$$\text{MAE} = \frac{1}{n}\sum_{i=1}^{n}|y_{mi} - y_i| \tag{30}$$

(5) R^2 represents the quality of a fitting through the change of data.

$$R^2 = 1 - \frac{\sum_{i=1}^{n}(y_{mi} - y_i)^2}{\sum_{i=1}^{n}(y_{mi} - \frac{1}{n}\sum_{i=1}^{n}y_{mi})^2} \tag{31}$$

In this work, four scenarios shown in Table III are studied. Since the scenarios of the WPTPS are characterized by wind speed, solar irradiance and the load, random variables $\beta_1, \beta_2, \beta_3$ and β_4 uniformly distribute on the intervals $[-0.5, 0.5]$, $[-50, 50]$, $[-75, 75]$, and $[-150, 150]$ respectively.

TABLE III
FOUR TYPICAL SCENARIOS IN THE TEST

Scenario	Group of time series data	Wind speed m/s	Solar irradiance W/m^2	Load disturbance MW
1	1000 in $\mathcal{D}_S$	$10+\beta_1$	$1000+\beta_2$	$1000+\beta_4$
2	50 in $\mathcal{D}_T$	$12+\beta_1$	$1000+\beta_2$	$1000+\beta_4$
	Current case	12	1000	1000+100
3	30 in $\mathcal{D}_T$	$10+\beta_1$	$800+\beta_2$	$1000+\beta_4$
	Current case	10	800	1000-100
4	20 in $\mathcal{D}_T$	$12+\beta_1$	$600+\beta_2$	$1000+\beta_3$
	Current case	12	600	1000-50

Scenario 1: The WPTPS operated at the initial state featured by the wind speed 10 m/s, solar irradiance 1000 W/m^2 and load 1000 MW. The uniformly distributed random disturbance was imposed on the wind speed, solar irradiance, and load respectively, whose perturbation ranges lie in [-0.5m/s, 0.5m/s], [-50W/m^2, 50W/m^2] and [-150MW, 150MW] respectively. The number of the hidden nodes is experimentally set to 10 for the pretrained RBFNNs and the initial weights of the RBFNNs are random numbers within a range [-1, 1]. 1000 groups input/output time series data of the WPTPS were collected and denoted as the data in the source domain $\mathcal{D}_S$. The collected input/output data in $\mathcal{D}_S$ were input to the RBFNNs, the pretrained SFR model can then be obtained. The average performance evaluation metrics are listed in Table IV. It is clear from Table IV that the pre-trained SFR model has high accuracy.

TABLE IV
AVERAGE PERFORMANCE EVALUATION METRICS OF PRETRAINED SFR MODEL

MSE	RMSE	SD	MAE	R^2
1.13e-9	3.36e-5	3.36e-5	2.29e-5	0.995

Scenario 2: The WPTPS operated in the vicinity of the operating point characterized by the wind speed 12m/s, solar irradiance 1000W/ m^2 and load 1000MW.

At the initial instant, the WPTPS run at the initial operating point featured by the wind speed 12m/s, solar irradiance 1000W/m^2 and load 1000MW. The uniformly distributed random disturbances were imposed on the wind speed, solar irradiance, and load respectively, whose perturbation ranges lie in [-0.5m/s, 0.5m/s], [-50W/m^2, 50 W/m^2], and [-150MW, 150MW] respectively. Fifty group input/output time series data of the WPTPS were collected and denoted as the data in the target domain $\mathcal{D}_T$. The transferred data can be obtained based on the MMD between $\mathcal{D}_S$ and $\mathcal{D}_T$. By adding hidden nodes to the frozen pretrained RBFNNs, the fine-tuned RBFNNs can be determined using the transferred data and the target data. Three additive hidden nodes were found by trial and error, and then the fine-tuned RBFNNs-based SFR model was obtained. For the WPTPS currently operating at the point (12m/s, 1000W/m^2, 1000MW), a positive 100MW load disturbance was imposed to the WPTPS disturbed by non-Gaussian wind speed and solar irradiance, the input/output time series data were input to the fine-tuned RBFNNs.

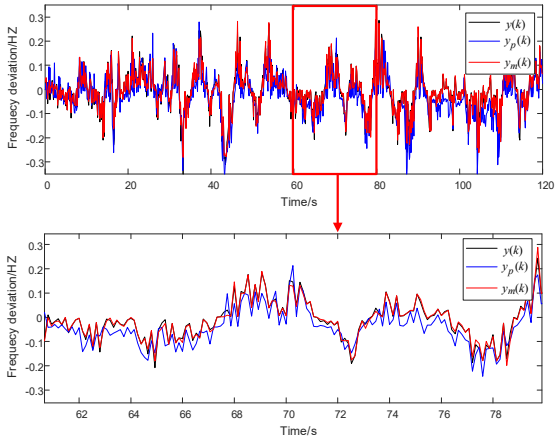

Fig. 7. Actual and identified frequency deviation via physical SFR model and fine-tuned SFR model.

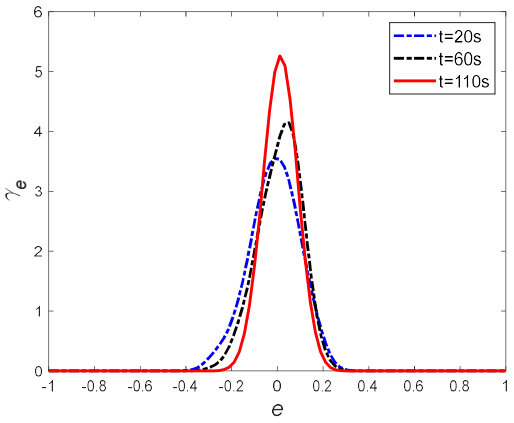

Fig. 8. The PDFs of the identification error γ_e at typical instants.

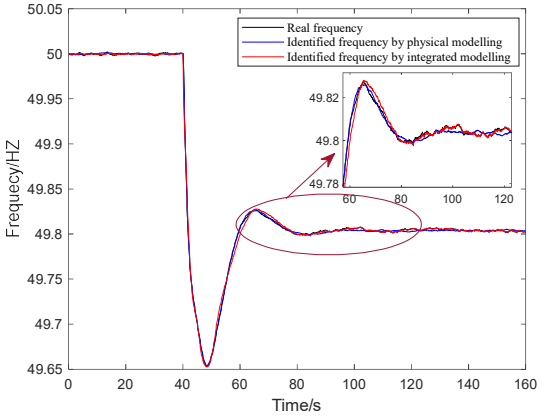

Fig. 9. Real and identified frequency by physical modelling and integrating modelling.

TABLE V
PERFORMANCE EVALUATION METRICS OF PHYSICAL MODELLING AND INTEGRATED MODELLING

Modelling method	MSE	RMSE	SD	MAE	R^2
Physical modelling	9.24e-8	3.04e-4	2.85e-4	2.47e-4	0.715
Integrated modelling	2.34e-9	4.83e-5	4.85e-5	3.31e-5	0.987

Figure 7 shows the actual frequency deviation $y(k)$, the identified frequency deviation $y_p(k)$ by physical modelling method, and the identified frequency deviation $y_m(k)$ by the integrated modelling method, respectively. The performance evaluation metrics are listed in Table V. Both Fig. 7 and Table V demonstrate that the proposed integrated modelling method obtained a more accurate identified frequency deviation than the physical modelling method. In addition, it is evident from Fig. 8 that the PDFs of the identification error γ_e obtained by the integrated modelling method are narrower and sharper. Figure 9 compares the identified results using two SFR modelling methods, the identified frequency obtained by integrating physical model and data-driven model is closer to the real frequency.

Scenario 3: The WPTPS operated in the vicinity of the operating point featured by wind speed 10m/s, solar irradiance 800W/m^2 and load 1000MW.

At the initial instant, the WPTPS operated at the initial operating point characterized by wind speed 10m/s, solar irradiance 1000W/m^2, and load 1000MW. The uniformly distributed random disturbances were imposed on wind speed, solar irradiance and load, respectively, whose perturbation ranges lie in [-0.5m/s, 0.5m/s], [-50W/m^2, 50 W/m^2], and [-150MW, 150MW] respectively. Three hidden nodes are experimentally added to the frozen pretrained RBFNNs and the fine-tuned RBFNNs-based SFR model is obtained. For the WPTPS currently operating at the point (10 m/s, 800W/㎡, 1000MW), a negative 100MW load disturbance was imposed on the WPTPS with non-Gaussian disturbances from wind speed and solar irradiance, the input/output time series data were input to the fine-tuned RBFNNs. Figure 10 demonstrates the identified frequency deviations obtained by physical modelling and integrated modelling method and the actual frequency deviation, respectively. The performance evaluation metrics are listed in Table VI.

It can be observed from both Fig. 10 and Table VI that the proposed SFR modelling method can obtain more accurate frequency deviation than physical modelling method. In addition, it is clear from Fig. 11 that the PDFs of the identification error γ_e obtained by the integrated modelling method become narrower and sharper gradually. Figure 12 validates that the proposed SFR modelling method can achieve better identification results.

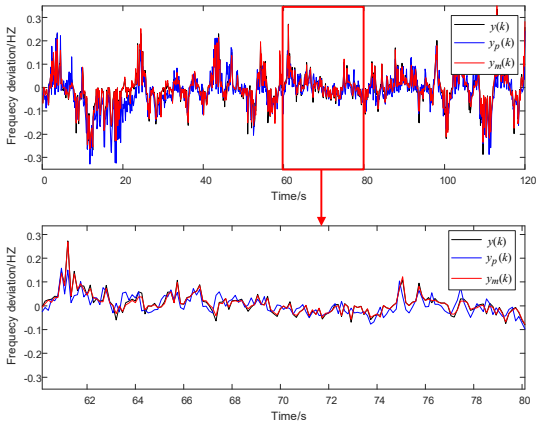

Fig. 10. Actual and identified frequency deviation via physical SFR model and fine-tuned SFR model.

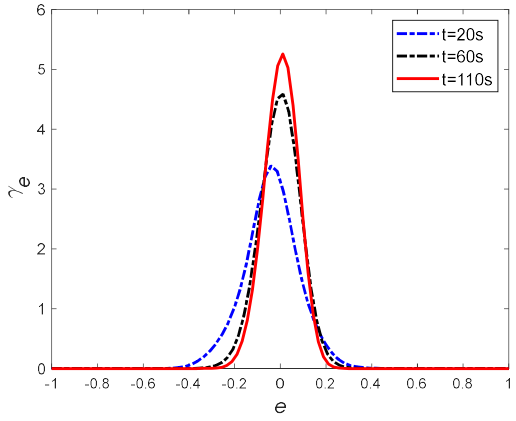

Fig. 11. PDFs of the identification error γ_e at typical instants.

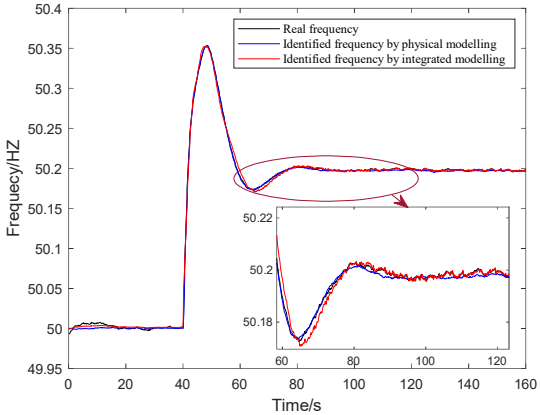

Fig. 12. Real and identified frequency by physical and integrating modelling.

TABLE VI
PERFORMANCE EVALUATION METRICS OF PHYSICAL MODELLING AND INTEGRATED MODELLING

Modelling method	MSE	RMSE	SD	MAE	R^2
Physical modelling	1.02e-7	3.19e-4	3.01e-4	2.58e-4	0.687
Integrated modelling	6.14e-9	7.84e-5	7.84e-5	5.93e-5	0.981

Scenario 4: The WPTPS operated in the vicinity of the operating point featured by wind speed 12 m/s, solar irradiance 600 W/m^2, and load 1000 MW.

At the initial instant, the WPTPS operated at the operating point featured by wind speed 12 m/s, solar irradiance 600 W/m^2, and load 1000 MW. The uniformly distributed random disturbances were imposed on wind speed, solar irradiance, and load, respectively, whose perturbation ranges are [-0.5m/s, 0.5m/s], [-50W/m^2, 50W/m^2], and [-75MW, 75MW] respectively. Four hidden nodes were found by trial and error and added to the frozen pretrained RBFNNs, consequently the fine-tuned SFR model is generated. For the WPTPS operating at the point (10m/s, 800W/m^2, 1000MW), a -50MW load step disturbance was imposed on the WPTPS with non-Gaussian disturbances induced by renewable energy sources. The input/output time series data were input to the fine-tuned RBFNNs.

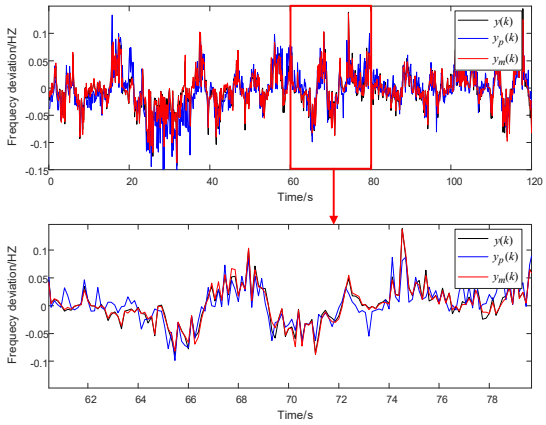

Fig. 13. Actual and identified frequency deviation via physical SFR model and fine-tuned SFR model.

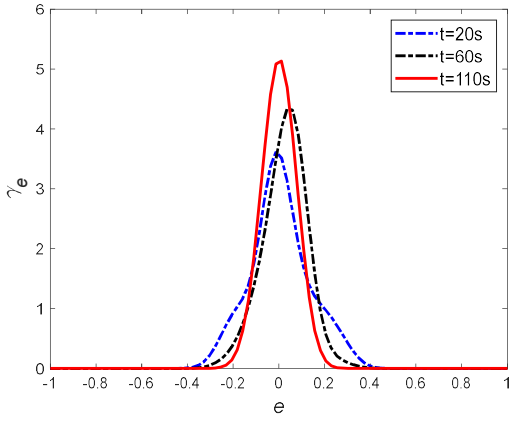

Fig. 14. PDFs of the identification error γ_e at typical instants

As shown in Fig. 13, the proposed SFR modelling method obtained better identified frequency deviation, which approaches the actual frequency deviation. The performance evaluation metrics are summarized in Table VII. Looking at both Fig. 13 and Table VII, it is apparent that the identified error approximates to zero using the proposed SFR modelling method. In addition, it can be seen from Fig. 14 that the PDFs of the identification error γ_e become narrow and sharp over time by using the proposed SFR modelling method. Fig. 15 also shows that the proposed SFR modelling approach outperforms the physical modelling method.

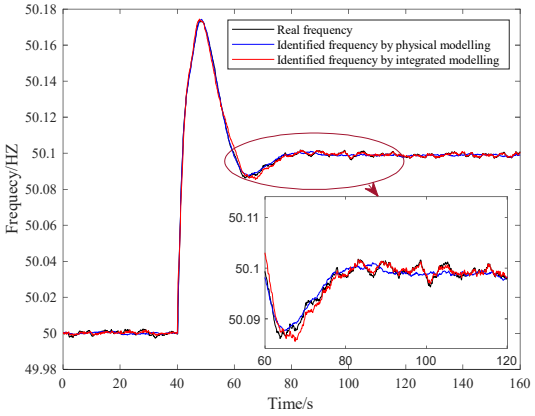

Fig. 15. Real frequency and identified frequency obtained by physical modelling and integrating modelling.

TABLE VII
PERFORMANCE EVALUATION METRICS OF PHYSICAL MODELLING AND INTEGRATED MODELLING

Modelling method	MSE	RMSE	SD	MAE	R^2
Physical modelling	9.32e-8	3.05e-4	2.87e-4	2.48e-4	0.713
Integrated modelling	2.47e-9	4.97e-5	4.97e-5	3.41e-5	0.984

V. CONCLUSIONS

In this paper, an integrated SFR modelling method is proposed for WPTPSs by combining physical modelling method and data-driven modelling method. In order to verify the proposed SFR modelling method, simulation tests are carried out in a WPTPS with different load, wind speeds and solar irradiances. The following conclusions can be drawn:

1) The BT method is applied to the equivalent low-order physical model rather than the high-order, high-fidelity model. The identification of the actual frequency deviation, as shown in simulation results, are pretty good. This shows the promising potential to apply the BT method to compute a lower-order approximation of the SFR model. Based on the reduced-order SFR physical model, the input nodes of the RBFNNs can be determined and the hidden nodes can then be decreased;

2) The pretrained modelling method is presented via the improved RBFNNs and TL. The SIP criterion is utilized to build an RBFNNs-based SFR model, which can deal with non-Gaussian disturbances in WPTPSs; Subsequently, the transferred source domain knowledge can be found based on the MMD criterion, and the fine-tuned SFR model can be obtained by increasing additive hidden nodes;

3) Transfer learning is employed to reduce the workload of data collection. If the MMD is too big, the transferred knowledge and the target data can't generate a satisfactory fine-

tuned SFR model. Accordingly, the pretrained SFR model should be modified using appropriate source data;

4) The established SFR model has a high identification accuracy and provides a way to analyze the SFR of WPTPSs with load, wind speed, and solar irradiance disturbances. The proposed modelling method can be extended to build the model of other processes or systems;

It is worth mentioning that the proposed SFR modelling method can build the SFR model for WPTPSs. Based on the SFR model, an adaptive primary frequency regulation strategy will be studied for WPTPSs in further research.

REFERENCES

[1] C. Seneviratne and C. Ozansoy, "Frequency response due to a large generator loss with the increasing penetration of wind/PV generation – A literature review", *Renew. Sust. Energ. Rev.*, vol. 57, pp. 659-668, 2016.

[2] D. Andrew, *Modern Aspects of Power System Frequency Stability and Control*, Western Pennsylvania Scholastic, WPS, USA: Academic Press; 2019.

[3] M. L. Chan, R. D. Dunlop and F. Schweppe, "Dynamic equivalents for average system frequency behaviour following major distribances," *IEEE Trans. Power Syst.*, vol. PAS-91, no. 4, pp. 1637-1642, July 1972.

[4] P. M. Anderson and M. Mirheydar, "A low-order system frequency response model," *IEEE Trans. Power Syst.*, vol. 5, no. 3, pp. 720-729, Aug. 1990.

[5] D. Lee, and H. Aik, "A general-order system frequency response model incorporating load shedding: analytic modeling and applications," *IEEE Trans. Power Syst.*, vol. 21, no. 2, pp. 709-717, May 2006.

[6] Q. Shi, F. Li and H. Cui, "Analytical method to aggregate multi-Machine SFR model with applications in power system dynamic studies," *IEEE Trans. Power Syst.*, vol. 33, no. 6, pp. 6355-6367, Nov. 2018.

[7] H. Ye, W. Pei and Z. Qi, "Analytical modeling of inertial and droop responses from a wind farm for short-term frequency regulation in power systems," *IEEE Trans. Power Syst.*, vol. 31, no. 5, pp. 3414-3423, Sept. 2016.

[8] M. Krpan and I. Kuzle, "Introducing low-order system frequency response modelling of a future power system with high penetration of wind power plants with frequency support capabilities," *IET Renew Power Gener*, vol. 12, no. 13, pp. 1453-1461, 1 10 2018.

[9] J. Dai, Y. Tang, Q. Wang, P. Jiang and Y. Hou, "An extended SFR model with high penetration wind power considering operating regions and wind speed disturbance," *IEEE Access*, vol. 7, pp. 103416-103426, 2019.

[10] D. Ochoa and S. Martinez, "Fast-frequency response provided by dfig-wind turbines and its impact on the grid," *IEEE Trans. Power Syst.*, vol. 32, no. 5, pp. 4002–4011, Sep. 2017.

[11] J. B. Hu, L. Sun, X. M. Yuan, S. Wang, and Y. N. Chi, "Modeling of type 3 wind turbines with df/dt inertia control for system frequency response study," *IEEE Trans. Power Syst.*, vol. 32, no. 4, pp. 2799-2809, Jul. 2017.

[12] H. Ahmadi and H. Ghasemi, "Security-constrained unit commitment with linearized system frequency limit constraints," *IEEE Trans. Power Syst.*, vol. 29, no. 4, pp. 1536–1545, Jul. 2014.

[13] Q. Li and M. E. Baran, "A novel frequency support control method for PV plants using tracking LQR," *IEEE Trans. Sustain. Energy*, vol. 11, no. 4, pp. 2263-2273, Oct. 2020.

[14] Y. Hain, R. Kulessky and G. Nudelman, "Identification-based power unit model for load-frequency control purposes," *IEEE Trans. Power Syst.*, vol. 15, no. 4, pp. 1313-1321, Nov. 2000.

[15] P. Huynh, H. Zhu, Q. Chen and A. E. Elbanna, "Data-driven estimation of frequency response from ambient synchrophasor measurements," *IEEE Trans. Power Syst.*, vol. 33, no. 6, pp. 6590-6599, Nov. 2018.

[16] Q. Bo, X. Wang and K. Liu, "Minimum frequency prediction of power system after disturbance based on the v-support vector regression," *POWERCON*, pp. 614-619, Oct. 2014.

[17] J. Zhang, H. Li, B. Hu, Y. Min, Q. Chen, G. Hou and C. Huang, "Modelling of SFR for wind-thermal power systems via improved RBF neural networks, "*Proceedings of CISC*, pp. 630-640, Sep. 2020.

[18] H. Li, P. Ju, C. Gan, S. You, F. Wu and Y. Liu, "Analytic analysis for dynamic system frequency in power systems under uncertain variability," *IEEE Trans. Power Syst.*, vol. 34, no. 2, pp. 982-993, March 2019.

[19] M. Malmström, *Uncertainties in neural networks: A system identification approach*, Linköping Studies in Science and Technology. Licentiate Thesis, No. 1902, 2021.

[20] S. A. Billings, *Nonlinear system identification: NARMAX methods in the time, frequency, and spatio-temporal domains*. John Wiley & Sons, Ltd, 2013, pp. 261-287.

[21] Z. Yun, Z. Quan, S. Caixin, L. Shaolan, L. Yuming and S. Yang," RBF neural network and ANFIS-based short-term load forecasting approach in real-time price environment," *IEEE Trans. Power Syst.*, vol. 23, no. 3, pp. 853-858, Aug. 2008.

[22] C. Cecati, J. Kolbusz, P. Różycki, P. Siano and B. M. Wilamowski, "A novel RBF training algorithm for short-term electric load forecasting and comparative studies," *IEEE Trans. Ind. Electron.*, vol. 62, no. 10, pp. 6519-6529, Oct. 2015.

[23] H. Han, L. Zhang, Y. Hou and J. Qiao, "Nonlinear model predictive control based on a self-organizing recurrent neural network," in *IEEE Trans. Neural Netw. Learn. Syst.*, vol. 27, no. 2, pp. 402-415, Feb. 2016

[24] L. Zhang, K. Li and E. Bai, "A new extension of newton algorithm for nonlinear system modelling using RBF neural networks," *IEEE Trans. Automat. Contr.*, vol. 58, no. 11, pp. 2929-2933, Nov. 2013.

[25] Y. Zhou and F. Ding, "Modeling nonlinear processes using the radial basis function-based state-dependent autoregressive models," *IEEE Signal Process. Lett.*, vol. 27, pp. 1600-1604, 2020.

[26] S. J. Pan and Q. Yang, "A survey on transfer learning," *IEEE Trans. Knowl. Data Eng.*, vol. 22, no. 10, pp. 1345-1359, Oct. 2010.

[27] F. Zhuang et al., "A comprehensive survey on transfer learning," *Proc. IEEE*, vol. 109, no. 1, pp. 43-76, Jan. 2021.

[28] S. Niu, Y. Liu, J. Wang and H. Song, "A decade survey of transfer learning (2010–2020)," *IEEE Trans. Artif. Intell.*, vol. 1, no. 2, pp. 151-166, Oct. 2020.

[29] P. Kundur, N. Balu and M. Lauby, *Power system stability and control.* New York: McGraw-Hill, 2009.

[30] S. Li, Y. Huang. X. Lei and C. Deng, "Modelling primary frequency regulation auxiliary control system of doubly fed induction generator based on rotor speed control." *Proceedings of the CSEE*, vol. 37, no. 24, pp. 7077-7086, Feb. 2017. (in Chinese)

[31] Zhao. D et al, "Research on control gain for photovoltaic power plants participating in primary frequency regulation of large power grid." *Power System Technology*, vol. 43, no. 2, pp. 425-433, Feb. 2019. (in Chinese)

[32] B. Moore, "Principal component analysis in linear systems: Controllability, observability, and model reduction," *IEEE Trans. Automat. Contr.*, vol. 26, no. 1, pp. 17-32, February 1981.

[33] B. Schäfer, C. Beck, K. Aihara, D. Witthaut and M. Timme, "Non-Gaussian power grid frequency fluctuations characterized by Lévy-stable laws and superstatistics", *Nat. Energy*, vol. 3, no. 2, pp. 119-126, 2018.

[34] L. Guo, Y. Yi, L. Yin and H. Wang, "Modelling, analysis and control theory of non-Gaussian random distribution system," *Science Press*, Beijing., 2019.

[35] Y. Li, J. Zhou, J. Tian, X. Zheng and Y. Tang, "Weighted error entropy-based information theoretic learning for robust subspace representation", *IEEE Trans. Neural Netw. Learn. Syst.*, pp. 1-15, 2021.

[36] B. Chen, P. Zhu and J. C. Principe, "Survival information potential: A new criterion for adaptive system training," *IEEE Trans. Signal Process.*, vol. 60, no. 3, pp. 1184-1194, March 2012.

[37] M. Ren, J. Chen, P. Shi, G. Yan, and L. Cheng, "Statistical information based two-layer model predictive control with dynamic economy and control performance for non-Gaussian stochastic process," *J Franklin Inst,* vol. 358, no. 4, pp. 2279-2300, Mar. 2021.

[38] L. Yin, L. Lai, Z. Zhu and T. Li, "Maximum power point tracking control for non-Gaussian wind energy conversion system by using survival information potential," *Entropy*, vol. 24, pp. 818. Jun. 2022.

[39] S. Schwendemann, Z. Amjad and A. Sikora, "Bearing fault diagnosis with intermediate domain based layered maximum mean discrepancy: A new transfer learning approach", *Eng. Appl. Artif. Intell.*, vol. 105, pp. 104415, 2021.

Jianhua Zhang received the B.Sc. degree in Industrial Automation from North China Electrical Power College, Hebei, China, in 1990, the M.Sc. degree in Control Engineering from Beijing graduate school of North China Electrical Power College, Beijing, China, in 1993, and the Ph.D. degree in mechanical engineering from Beijing University of Aeronautics and Astronautics, Beijing, China, in 1996.

She is currently a Professor in the School of Control and Computer Engineering, North China Electric Power University, Beijing. Her research interests include the areas of integrated energy systems, stochastic control, networked control systems, power system and process control.

Yongyue Wang received the B.Sc. degree in Control Theory and Control Engineering from North China Electric Power University, Beijing, China, in 2020.

He is currently pursuing the Ph.D. degree in Control Theory and Control Engineering from North China Electric Power University. His research interests include hybrid power system, frequency regulation, neural networks, robust control, stochastic control and intelligent optimization.

Guiping Zhou received the B.Sc. degree in Dalian University of Technology, Dalian, China, in 2004, the M.Sc. degree in Shenyang University of Chemical Technology, Shenyang, China, in 2007, and the Ph.D. degree in Shenyang Institute of Automation Chinese Academy of Sciences, Shenyang, China, in 1995.

He is currently working at the State Grid Liaoning Electric Power Supply Co. Ltd. His research interests include power system and automation.

Lei Wang received the B.Sc. degree in Harbin Engineering University, Harbin, China, in 2004, the M.Sc. degree and the Ph.D. degree in Harbin Institute of Technology, Harbin, China, in 2007, and 2011, respectively.

He is currently working at the State Grid Liaoning Electric Power Supply Co. Ltd. His research interests include network security management, network security architecture protection design, network and information security technology.

Bin Li received the B.Sc. degree and the M.Sc. degree in College of Information Science and Engineering from Northeastern University, Shenyang, China, in 2004, and 2008, respectively, and the Ph.D. degree in School of Electrical Engineering from Shenyang University of Technology, Shenyang, China, in 2013.

He is currently working at the State Grid Liaoning Electric Power Supply Co. Ltd. His research interests include grid equipment status detection and fault diagnosis.

Kang Li (M'05–SM'11) received the B.Sc. degree in Industrial Automation from Xiangtan University, Hunan, China, in 1989, the M.Sc. degree in Control Theory and Applications from Harbin Institute of Technology, Harbin, China, in 1992, and the Ph.D. degree in Control Theory and Applications from Shanghai Jiaotong University, Shanghai, China, in 1995. He also received D.Sc. degree in Engineering from Queen's University Belfast, UK, in 2015.

Between 1995 and 2002, he worked at Shanghai Jiaotong University, Delft University of Technology and Queen's University Belfast as a research fellow. Between 2002 and 2018, he was a Lecturer (2002), a Senior Lecturer (2007), a Reader (2009) and a Chair Professor (2011) with the School of Electronics, Electrical Engineering and Computer Science, Queen's University Belfast, Belfast, U.K. He currently holds the Chair of Smart Energy Systems at the University of Leeds, UK. His research interests cover nonlinear system modelling, identification, and control, and machine learning, with substantial applications to energy and power systems, smart grid, transport decarbonization, and energy management in energy intensive manufacturing processes. He has authored/co-authored over 200 journal publications and edited/co-edited 18 conference proceedings, winning over 20 prizes and awards, including Springer Nature 'China New Development Award' in 2019 in recognition of the 'exceptional contributions to the delivery of the UN Sustainable Development Goals'.

Dr Li was the Chair of the IEEE UKRI Control and Communication Ireland chapter, the Secretary of the IEEE UK & Ireland Section. He is also a visiting professor of Shanghai Jiaotong University, Southeast University, Tianjin University, Shanghai University and Xiangtan University.